Journal of Materials Chemistry C

ROYAL SOCIETY OF CHEMISTRY

PAPER

View Article Online
View Journal | View Issue

Cite this: J. Mater. Chem. C, 2020, 8, 2314

Solution processed red organic light-emitting-diodes using an *N*-annulated perylene diimide fluorophore†

Sergey V. Dayneko,[a] Mohammad Rahmati,[b] Majid Pahlevani*[c] and Gregory C. Welch *[a]

Received 11th October 2019,
Accepted 5th January 2020

DOI: 10.1039/c9tc05584c

rsc.li/materials-c

In this contribution we report on solution processed red OLEDs based upon an *N*-annulated perylene diimide dimer, namely tPDI$_2$N-EH, a red-light emitting molecule. OLED devices with the architecture of glass/ITO/PEDOT:PSS/EML/LiF/Ag (EML = emitting layer) were fabricated with EMLs comprised of tPDI$_2$N-EH neat and blended with poly(9,9-dioctylfluorene, PFO), all solution processed from non-halogenated solvents. The photophysical and electrophysical performance of PFO:tPDI$_2$N-EH-blend films with different composition ratios were investigated. The PFO : tPDI$_2$N-EH-based OLEDs with a 2 : 18 ratio exhibited the best performance. The PFO:tPDI$_2$N-EH-based OLEDs gave red electroluminescence with the emission wavelength of 635 nm and the CIE (international commission on illumination) coordinates of (x = 0.672, y = 0.321). OLEDs with EMLs fabricated using roll-to-roll compatible methods are also demonstrated.

1. Introduction

Organic light-emitting diodes (OLEDs) have successfully been deployed in light fixtures, mobile phones, and televisions over the past few years owing to continued improvements in both performance and lifetimes.[1–5] OLEDs are multilayer devices with each layer having a distinct function including charge-injection, charge-transport, and light emission. The active emissive layer (EML) dictates the colour and maximum efficiency of OLEDs. For solution processing of electronically active layers; spin-coating,[6] roll-to-roll coating[7] and inkjet printing[8] are the most common methods used. Solution processing is more challenging than thermal evaporation due to difficulties in forming distinct layers one on top of each other without bleeding or swelling. In support of solution processing it has been demonstrated that solution processed OLEDs can match the performance of thermally evaporated OLEDs.[9] To create high-performance solution-processed OLEDs both conjugated polymers[10] and small molecules[11] have been used as the core component of the EML.

To date, the efficiency and purity of red colour solution processed OLEDs remains behind that of other coloured OLEDs (*i.e.* blue, green and orange).[12] This is primarily a result of low-energy fluorescence being competitive with non-radiative decay pathways.[13] Most high efficient red-emitting materials are organometallic in nature[14] and suffer from high costs and poor environmental stability. The design of new metal-free organic small molecules is a viable route towards low-cost, high-performance, large area red OLEDs.[15]

The perylene diimide (PDI) chromophore is an excellent building block for which to construct new emitters for solution-processed red OLEDs owing to a pure red colour, high quantum yield photoluminescence, and high thermal and photochemical stability.[16–18] Furthermore, PDIs can be rendered soluble in a range of both polar and non-polar solvents and thus are suitable for large area roll-to-roll coating.[19–21] PDI-based materials have found wide utility as active materials in transistors,[22,23] solar cells[24,25] and OLEDs.[26–28] PDI-based OLEDs typically have pure deep red electroluminescence with the emission wavelength of 690 nm and CIE coordinates of (x = 0.69, y = 0.29).[26] For example, stable red emission from a PDI-based OLED with an external quantum efficiency of 4.93% has been demonstrated.[29]

Here, we report red OLEDs based on an emissive dimeric PDI, namely tPDI$_2$N-EH. This compound is an *N*-annulated PDI dimer that has found utility as a non-fullerene acceptor for organic photovoltaics.[30] Blending tPDI$_2$N-EH with polyfluorene based polymers and used as the EML lead to good-performance OLED devices. The optical and electrophysical properties of PFO:tPDI$_2$N-EH blended films were studied. The best PFO:tPDI$_2$N-EH blend OLEDs were compared with standard OLEDs based on PFO:F8BT blend films (F8BT = poly[(9,9-di-*n*-octylfluorenyl-2,7-diyl)-*alt*-(benzo[2,1,3]thiadiazol-4,8-diyl)]). Best devices were fabricated by slot-die coating, a roll-to-roll compatible method, as proof-of-concept.

[a] Department of Chemistry, University of Calgary, 731 Campus Place NW, Calgary, Alberta, Canada T2N 1N4. E-mail: gregory.welch@ucalgary.ca
[b] Genoptic LED Inc., 6000 72nd Ave SE, Calgary, AB, Canada T2C 5B1
[c] Department of Electrical and Computer Engineering, Queen's University, 19 Union St., Kingston, ON, Canada K7L 3N6. E-mail: majid.pahlevani@queensu.ca

† Electronic supplementary information (ESI) available. See DOI: 10.1039/c9tc05584c

2. Results and discussion

2.1 Materials selection

The *N*-annulated PDI dimer, tPDI$_2$N-EH (Fig. 1a),[30] can be synthesized on multi-gram scale, is semiconducting, and can be coated *via* roll-to-roll processes from non-halogenated solvents.[19,20] It has a red luminescence peak at 650 nm (Fig. 1b) and is chemically stable as a film in sunlight. Thus, this material is appropriate for use as a solution processable light emitter. The luminescent conjugated polymers PFO and F8BT (structures are shown in Fig. 1a) were selected as a hole transporter and control emitter, respectively, since they exhibit high light stability[31] and consistent performance as light emitters in OLEDs.[32–35] A recent report has shown that PFO:F8BT-ink formulations are suitable to be slot-die coated into an OLED structure.[36] PFO:F8BT based OLEDs were fabricated as control devices. The PFO polymer is p-type with appropriate electronic energy levels to pair with the F8BT or tPDI$_2$N-EH to facilitate hole transport (Fig. 1c). Moreover, the wavelengths of the tPDI$_2$N-EH absorption and PFO luminescence overlap (Fig. 1b and Fig. S1, ESI†) enabling Förster Resonance Energy Transfer (FRET) to occur from PFO to tPDI$_2$N-EH. This makes the PFO:tPDI$_2$N-EH system an excellent candidate as a OLED EML.

2.2 OLEDs – spin-coated devices

Device fabrication and characterization. OLED devices with the structure of glass/ITO/PEDOT:PSS/EML/LiF/Ag were fabricated and tested under ambient conditions. Control devices with an EML of PFO : F8BT-blend film were spin-cast from toluene with the ratio of 19 : 1 at 15 mg mL^{-1}. EMLs comprised of PFO : tPDI$_2$N-EH-blend films were spin-cast from toluene at different ratios (from 19 : 1 to 1 : 19). The full details of the fabrication technique can be found in the ESI.† Electrical characterization of the devices was performed with a Keithley 2612B source-meter combined with the calibrated Si-photodiode and spectrometer.

Photophysical properties of the PFO:tPDI$_2$N-EH films. The optical absorption and photoluminescence (PL) spectra of PFO:tPDI$_2$N-EH-blend films are shown in Fig. 2 (PL data tabulated in Table 1). The absorption band from 330 nm to 430 nm is attributed to PFO and from 450 nm to 650 nm is attributed to tPDI$_2$N-EH. Changing the ratio from 19 : 1 to 1 : 19 (PFO : tPDI$_2$N-EH) results in an expected decrease/increase of the PFO/tPDI$_2$N-EH absorption bands with no significant changes in shape or position of each spectrum (Fig. 2a).

Excitation at 400 nm (near peak absorption of PFO) of blended films with the ratios of 19 : 1 and 18 : 2 yields spectra with quenched emission of PFO (from 430–500 nm) and longer wave emission from 600–750 nm which is attributed with tPDI$_2$N-EH. The quenched PL of PFO is associated with FRET from PFO to tPDI$_2$N-EH. Increasing the concentration of tPDI$_2$N-EH in blend films leads to complete quenching of the PFO light emission (at a ratio from 15 : 5 to 1 : 19) and increased PL of tPDI$_2$N-EH compared to neat film (Fig. 2b).

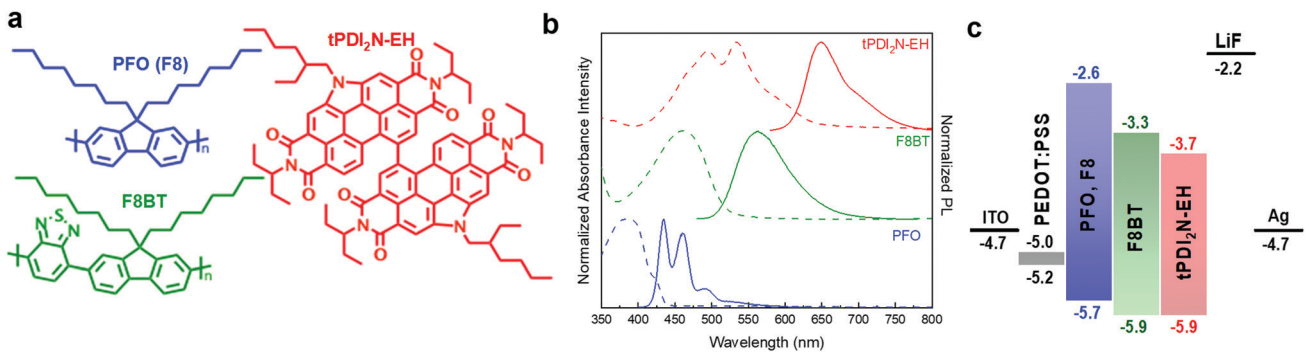

Fig. 1 (a) Chemical structures of the polymers PFO (F8) and F8BT, and the small molecule tPDI$_2$N-EH used in this study. (b) Normalized absorption and photoluminescence spectra of PFO (blue dash and solid line), F8BT (green dash and solid line), and tPDI$_2$N-EH (red dash and solid line) films spin-cast from toluene at 15 mg mL^{-1} under λ_{ex} = 350 nm, 400 nm and 530 nm, respectively. (c) Energy level diagram with values for organic materials (energy levels taken from the relevant literature, the PEDOT:PSS has a work function of 5.0–5.2 eV).

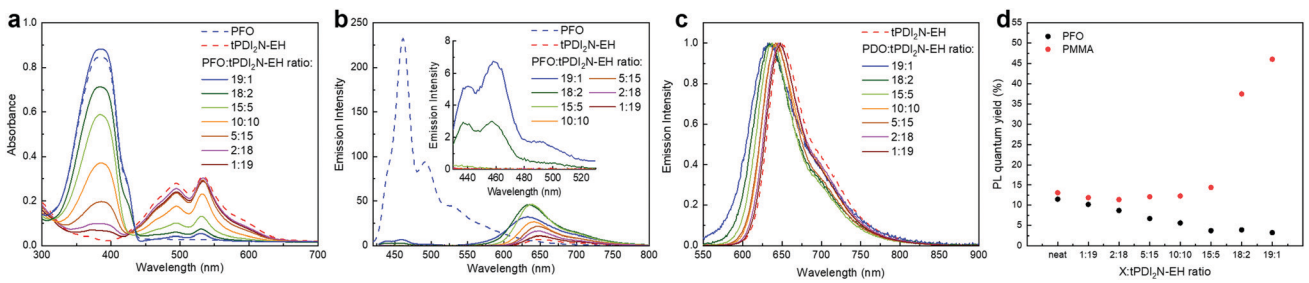

Fig. 2 (a) Optical absorption and (b and c) photoluminescence spectra of PFO:tPDI$_2$N-EH-blend and neat films spin-cast from toluene at 15 mg mL^{-1} under (b) λ_{ex} = 400 nm and (c) λ_{ex} = 530 nm. (d) PL quantum yield (QY) values of X:tPDI2-EH (X = PFO or PMMA) blend films with different ratio. Excitation wavelengths for PLQY measurements was 530 nm.

Table 1 Optical properties of $tPDI_2N$-EH and PFO:$tPDI_2N$-EH-blend films

		Emission of $tPDI_2N$-EH				
		Under λ_{ex} = 400 nm		Under λ_{ex} = 530 nm		
Compounds	PFO : $tPDI_2N$-EH ratio	Max.	FWHW[a]	Max.	FWHM[a]	QY[b], %
PFO : $tPDI_2N$-EH	19 : 1	633	77	633	75	3.2
PFO : $tPDI_2N$-EH	18 : 2	635	63	636	62	3.9
PFO : $tPDI_2N$-EH	15 : 5	639	55	638	55	3.7
PFO : $tPDI_2N$-EH	10 : 10	641	57	642	57	5.6
PFO : $tPDI_2N$-EH	5 : 15	645	54	644	55	6.7
PFO : $tPDI_2N$-EH	2 : 18	646	57	647	60	8.7
PFO : $tPDI_2N$-EH	1 : 19	648	56	647	57	10.2
$tPDI_2N$-EH	—	653	60	650	60	11.5

[a] FWHM – full width at half maximum; $tPDI_2N$-EH and PFO:$tPDI_2N$-EH-blend films was spin-cast on glass from toluene at 15 mg mL^{-1}. [b] The absolute photoluminescence quantum yield of films.[37]

Excitation at 530 nm of blended films results in only one emission band from 600–750 nm, a result of PL from $tPDI_2N$-EH (Fig. 2c). The blue-shift in PL spectra of $tPDI_2N$-EH (from 650 nm to 630 nm) with increasing PFO concentration is the result of decreased aggregation of the $tPDI_2N$-EH molecules. However, PL quantum yield (PLQY) of PFO:$tPDI_2N$-EH-blend films is decreasing from 11.5% (neat film) to 3.2% (ratio 19 : 1) (Fig. 2d). On the other hand, the PLQY of $tPDI_2N$-EH dispersed in a poly(methyl methacrylate) (PMMA) matrix increased up to 46% (ratio 19 : 1) as shown in Fig. 2d. Thus, quenching of the $tPDI_2N$-EH PL in the PFO polymer film is associated with charge dissociation between PFO and $tPDI_2N$-EH. Nevertheless, PFO plays an important role in the PFO:$tPDI_2N$-EH-based OLEDs since it improves charge injection into EML and is involved in energy transfer processes. Importantly, the PFO has the smallest effect on the PLQY of $tPDI_2N$-EH from 1 : 19 to 10 : 10 ratio, which is preferred for development of OLEDs.

OLED devices. OLED device characteristics based on $tPDI_2N$-EH and PFO:$tPDI_2N$-EH-blend films with different ratios are shown in Fig. 3 and Table 2; the data include graphics of current density–voltage curves (*J*–*V*, Fig. 3a), luminance *versus* applied voltage curves (*L*–*V*, Fig. 3b) and luminous efficiency *versus* current density curves (LE–*J*, Fig. 3c). The OLEDs based on only $tPDI_2N$-EH films as the EML showed a maximum luminous efficiency (LE) of around 4×10^{-3} cd A^{-1} with a maximum brightness of 4.1 cd m^{-2}, which agree well with the previously obtained data for other PDI-based OLEDs.[26] The highest performance OLEDs were based on PFO : $tPDI_2N$-EH EML with the blend ratio of 2 : 18 and had the maximum LE of 0.05 cd A^{-1}, power efficiency (PE) of 0.03 lm W^{-1}, and external quantum efficiency (EQE) of 0.06%. Increasing the concentration of PFO in PFO:$tPDI_2N$-EH-blend leads to performance deterioration of the fabricated OLEDs, which agrees well with the PL data (Fig. S2, ESI†). The turn-on voltage of the $tPDI_2N$-EH-based OLEDs decreases when

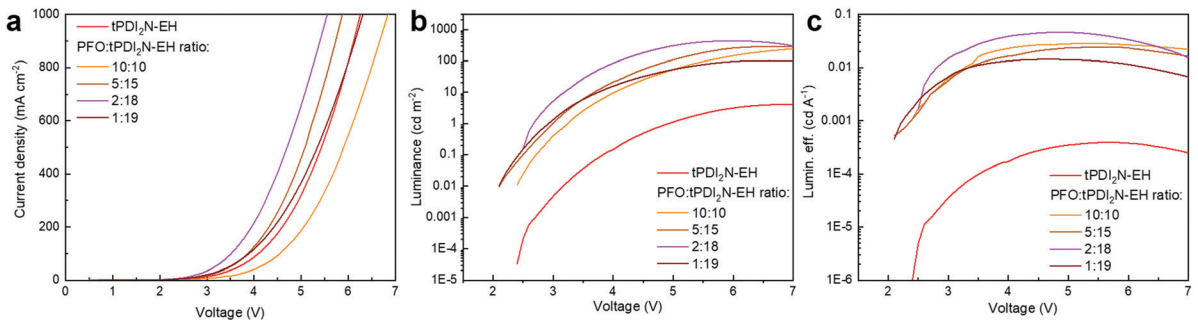

Fig. 3 (a) Current density–voltage (*J*–*V*) characteristics, (b) luminance *versus* applied voltage (*L*–*V*, cd m^{-2}) and (c) luminous efficiency (lumin. eff.) *versus* current density (LE–*J*, cd A^{-1}) of PFO:$tPDI_2N$-EH OLEDs at selected ratios.

Table 2 Summary of device performance for OLEDs based on $tPDI_2N$-EH and PFO:$tPDI_2N$-EH-blend films with different ratio spin-coated on the glass

Emitting layer	Ratio[a]	V_{on}[b] [V]	EQE_{max}[c] [%]	LE_{max}[d] [cd A^{-1}]	PE_{max}[e] [lm W^{-1}]	L_{max}[f] [cd m^{-2}]
$tPDI_2N$-EH	—	4.9	0.000504	0.000392	0.000236	4.1
PFO : $tPDI_2N$-EH	10 : 10	3.2	0.035	0.028	0.019	262.3
PFO : $tPDI_2N$-EH	5 : 15	3.0	0.031	0.025	0.015	288.5
PFO : $tPDI_2N$-EH	2 : 18	2.6	0.057	0.046	0.031	435.4
PFO : $tPDI_2N$-EH	1 : 19	2.7	0.018	0.014	0.010	101.8

[a] PFO : $tPDI_2N$-EH ratio. [b] Turn on voltage was determined at the brightness of 1 cd m^{-2}. [c] EQE – external quantum efficiency. [d] LE – luminous efficiency. [e] PE – power efficiency. [f] L_{max} – maximum of luminous.

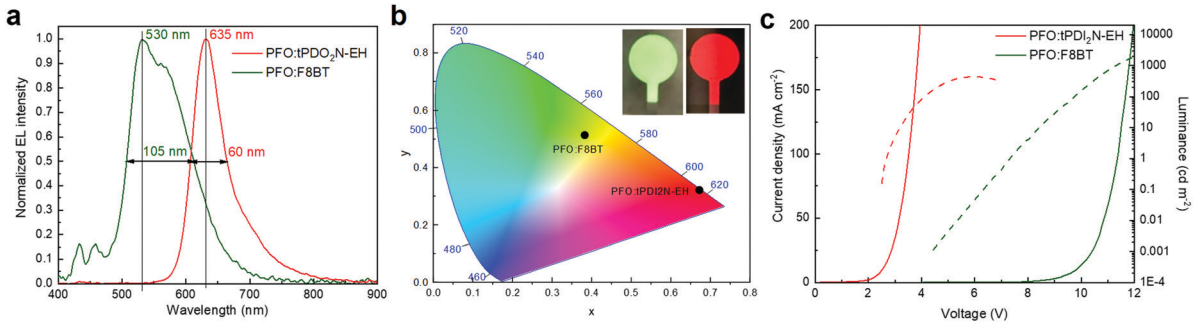

Fig. 4 (a) Normalized electroluminescence (EL) and (b) color coordinates spectra, (c) current–voltage–luminance characteristics of PFO : F8BT (ratio 19 : 1) and PFO : $tPDI_2N$-EH (ratio 2 : 18) blends.

Table 3 Summary of device performance for OLEDs based on PFO:F8BT and PFO:$tPDI_2N$-EH-blend films spin-coated on glass

Emitting layer	Ratio[a]	V_{on}[b] [V]	EQE_{max}[c] [%]	LE_{max}[d] [cd A^{-1}]	PE_{max}[e] [lm W^{-1}]	L_{max}[f] [cd m^{-2}]
PFO : F8BT	19 : 1	7.3	0.406	1.24	0.376	1951.6
PFO : $tPDI_2N$-EH	2 : 18	2.6	0.057	0.046	0.031	435.4

[a] PFO : F8BT or PFO : $tPDI_2N$-EH ratio. [b] Turn on voltage was determined at the brightness of 1 cd m^{-2}. [c] EQE – external quantum efficiency. [d] LE – luminous efficiency. [e] PE – power efficiency. [f] L_{max} – maximum of luminous.

PFO is added to the EML. Adding the PFO, which has a higher lying HOMO energy level than $tPDI_2N$-EH, helps facilitate hole injection from PEDOT:PSS to the EML. The turn-on voltage of 2.6 V for the OLEDs with PFO:$tPDI_2N$-EH EMLs is the lowest reported for PDI-based OLEDs.[26,27,29,38]

OLED electroluminescence. The electroluminescence (EL), CIE, and current–voltage–luminance characteristics of standard PFO : F8BT (19 : 1 ratio) and optimized PFO : $tPDI_2N$-EH-based (2 : 18 ratio) OLEDs are shown in Fig. 4 and Table 3. PFO:F8BT-based OLEDs demonstrated the maximum LE of 1.24 cd A^{-1}, PE of 0.4 lm W^{-1} and brightness of 1950 cd m^{-2} with white-green spectrum at maximum of 530 nm, full width at half maximum (FWHM) of 105 nm, and CIE coordinates located at (x, y) = (0.383, y = 0.514). This data is well aligned with literature.[33,36] Using $tPDI_2N$-EH instead of F8BT with PFO shifts the EL to red, which agrees well with the PL of $tPDI_2N$-EH. The PFO:$tPDI_2N$-EH-based OLEDs exhibit a narrow peak of EL with the maximum emission at 635 nm and FWHM of 60 nm with the CIE coordinates of (x, y) = (0.672, 0.321). Moreover, using $tPDI_2N$-EH decreases the turn-on voltage to 2.6 V due to the lower LUMO energy level and more facile injection of electrons from the contacts into the active layer.

2.3 OLEDs – slot-die coated devices

The roll-to-roll compatibility of organic and inorganic layers of OLED devices is an important consideration for large-scale fabrication methods.[7] Thus, we aimed to repeat our best spin-coated devices with a slot-die coating technique. A FOM Nano Roll Coater (slot-die head with 13 mm shim width) was used to coat both the PEDOT : PSS interlayer and PFO : $tPDI_2N$-EH (2 : 18) EML onto a PET/ITO substrate/anode base. The PEDOT:PSS interlayer was slot-die coated with the coating speed of 0.1 mm^{-1}, dispensing rate of 12 μL min^{-1}, and substrate temperature of 50 °C. The layer was thermally annealed at 100 °C for 15 min prior to the deposition of the EML. The PFO : $tPDI_2N$-EH (2 : 18) solutions were coated from toluene at 30 mg mL^{-1} with the coating speed of 0.3 mm^{-1}, dispensing rate of 30 μL min^{-1} at room temperature. The films were then dried in air at 100 °C for 30 minutes. A LiF/Ag electrode was thermally deposited using a thermal evaporation

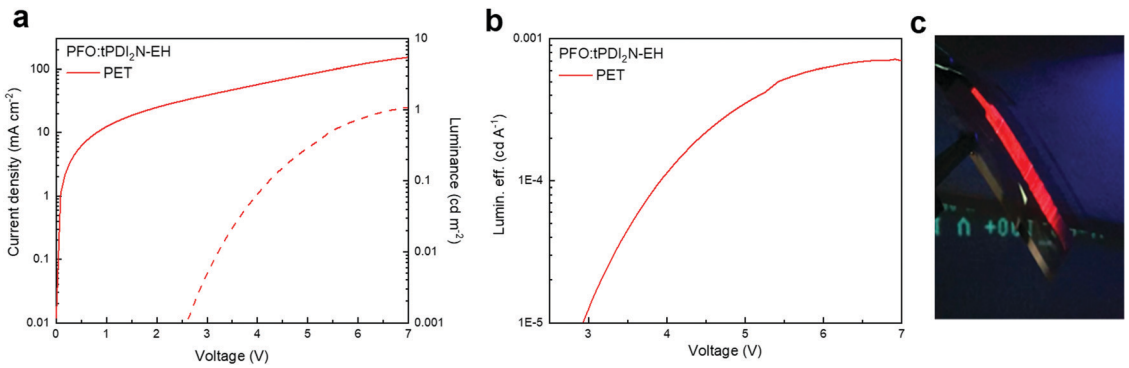

Fig. 5 (a) Current–voltage–luminance characteristics and (b) luminous efficiency (lumin. eff.) *versus* current density (LE–J, cd A^{-1}) of PFO:$tPDI_2N$-EH roll-to-roll coated on PET. (c) Photo of electroluminescent of PFO:$tPDI_2N$-EH OLEDs on PET.

Table 4 Summary of device performance for slot-die coating OLEDs based on PFO:tPDI$_2$N-EH-blend films

Emitting layer	Substrate	V_{on}[b] [V]	EQE_{max}[c] [%]	LE_{max}[d] [cd A^{-1}]	PE_{max}[e] [lm W^{-1}]	L_{max}[f] [cd m^{-2}]
PFO : tPDI$_2$N-EH[a]	PET/ITO[g]	6.6	0.000147	0.000718	0.000054	1.1

[a] PFO : tPDI$_2$N-EH ratio is 2 : 18. [b] Turn on voltage was determined at the brightness of 1 cd m^{-2}. [c] EQE – external quantum efficiency. [d] LE – luminous efficiency. [e] PE – power efficiency. [f] L_{max} – maximum of luminous. [g] The EML prepared from a solvent of toluene by roll-to-roll coated with the active area 160 mm^2.

system through a shadow mask under a base pressure of $\sim 2 \times 10^{-6}$ Torr (this top electrode was used for consistency in comparing to the spin-coated OLEDs). The device area was 160 mm^2 as defined by the overlapping area of the ITO films and top electrodes. The optical absorption spectra of the roll-to-roll coated devices (in comparison to the spin-coated ones) can be found in the ESI† (Fig. S3).

The current–voltage–luminance characteristics and LE *versus* current density of OLED devices with the PEDOT:PSS and PFO:tPDI$_2$N-EH layers roll-to-roll coated on PET are shown in Fig. 5 and electrophysical parameters are summarized in Table 4. The OLED had a turn-on voltage of 6.6 V and maximum brightness of 1.1 cd m^{-2}, demonstrating a fully functioning large area, roll-to-roll compatible coated device. Thus, this work shows that large-area OLEDs can be fabricated using slot-die coating techniques. The synthesis of new PDIs with high quantum yield and narrow peak luminescence of films, and optimized roll-to-roll coating of OLED layers is a viable pathway towards developing high-performance OLEDs for large-scale manufacturing.

3. Conclusion

We have presented electrically pumped, solution processed red OLEDs based on an *N*-annulated perylene diimide dimer as the emitting material. Use of the polyfluorene based polymer PFO as an additive for the red-emitter tPDI$_2$N-EH resulted in large performance boosts with an optimal PFO : tPDI$_2$N-EH ratio of 2 : 18 identified. The best efficiencies of PFO:tPDI$_2$N-EH-based OLEDs exhibited a maximum LE of 0.05 cd A^{-1}, power efficiency (PE) of 0.03 lm W^{-1} and external quantum efficiency (EQE) of 0.06%, and are among the best for PDI-based OLEDs. Proof-of-concept large-scale fabrication of OLEDs was demonstrated by roll-to-roll compatible coating of both the PEDOT:PSS hole injection layer and PFO:tPDI2N-EH emitting layer of OLEDs with large area (160 mm^2) on plastic substrates. This work highlights the potential of *N*-annulated perylene diimide based materials to deliver commercially relevant advanced lighting devices.

Conflicts of interest

There are no conflicts to declare.

Acknowledgements

GCW acknowledges CFI JELF (34102), CRC, WED, and the University of Calgary. SVD is grateful for a MITACS fellowship. Authors would like to thank GenOptic LED Inc. for their financial support.

References

1 H.-W. Chen, J.-H. Lee, B.-Y. Lin, S. Chen and S.-T. Wu, *Light Sci. Appl.*, 2018, **7**, 17168.
2 J. Ràfols-Ribé, P.-A. Will, C. Hänisch, M. Gonzalez-Silveira, S. Lenk, J. Rodríguez-Viejo and S. Reineke, *Sci. Adv.*, 2018, **4**, eaar8332.
3 N. B. Kotadiya, P. W. M. Blom and G.-J. A. H. Wetzelaer, *Nat. Photonics*, 2019, **13**, 765–769.
4 K. Guo, H. Wang, Z. Wang, C. Si, C. Peng, G. Chen, J. Zhang, G. Wang and B. Wei, *Chem. Sci.*, 2017, **8**, 1259–1268.
5 S. Sato, S. Ohisa, Y. Hayashi, R. Sato, D. Yokoyama, T. Kato, M. Suzuki, T. Chiba, Y. Pu and J. Kido, *Adv. Mater.*, 2018, **30**, 1705915.
6 B. R. Lee, E. D. Jung, J. S. Park, Y. S. Nam, S. H. Min, B.-S. Kim, K.-M. Lee, J.-R. Jeong, R. H. Friend, J.-S. Kim, S. O. Kim and M. H. Song, *Nat. Commun.*, 2014, **5**, 4840.
7 A. Sandström, H. F. Dam, F. C. Krebs and L. Edman, *Nat. Commun.*, 2012, **3**, 1002.
8 C. Amruth, M. Z. Szymański, B. Łuszczyńska and J. Ulański, *Sci. Rep.*, 2019, **9**, 8493.
9 V. G. Sree, H. Park, W. Cho and S.-H. Jin, *Mol. Cryst. Liq. Cryst.*, 2017, **654**, 73–82.
10 S. Burns, J. MacLeod, T. Trang Do, P. Sonar and S. D. Yambem, *Sci. Rep.*, 2017, **7**, 40805.
11 N. Aizawa, Y.-J. Pu, M. Watanabe, T. Chiba, K. Ideta, N. Toyota, M. Igarashi, Y. Suzuri, H. Sasabe and J. Kido, *Nat. Commun.*, 2014, **5**, 5756.
12 Q. Wei, N. Fei, A. Islam, T. Lei, L. Hong, R. Peng, X. Fan, L. Chen, P. Gao and Z. Ge, *Adv. Opt. Mater.*, 2018, **6**, 1800512.
13 Q. Zhang, H. Kuwabara, W. J. Potscavage, S. Huang, Y. Hatae, T. Shibata and C. Adachi, *J. Am. Chem. Soc.*, 2014, **136**, 18070–18081.
14 H. Xiang, J. Cheng, X. Ma, X. Zhou and J. J. Chruma, *Chem. Soc. Rev.*, 2013, **42**, 6128.
15 Q. Zhao and J. Z. Sun, *J. Mater. Chem. C*, 2016, **4**, 10588–10609.
16 D. Schmidt, M. Stolte, J. Süß, A. Liess, V. Stepanenko and F. Würthner, *Angew. Chem., Int. Ed.*, 2019, **58**, 13385–13389.
17 R. P. Sabatini, B. Zhang, A. Gupta, J. Leoni, W. W. H. Wong and G. Lakhwani, *J. Mater. Chem. C*, 2019, **7**, 2954–2960.
18 B. Zhang, H. Soleimaninejad, D. J. Jones, J. M. White, K. P. Ghiggino, T. A. Smith and W. W. H. Wong, *Chem. Mater.*, 2017, **29**, 8395–8403.
19 A. Laventure, C. R. Harding, E. Cieplechowicz, Z. Li, J. Wang, Y. Zou and G. C. Welch, *ACS Appl. Polym. Mater.*, 2019, **1**, 2168–2176.
20 F. Tintori, A. Laventure and G. C. Welch, *ACS Appl. Mater. Interfaces*, 2019, **11**, 39010–39017.

21 A. Laventure, S. Stanzel, A.-J. Payne, B. H. Lessard and G. C. Welch, *Synth. Met.*, 2019, **250**, 55–62.
22 R. K. Gupta, A. Dey, A. Singh, P. K. Iyer and A. A. Sudhakar, *ACS Appl. Electron. Mater.*, 2019, **1**, 1378–1386.
23 G. Li, D. Li, X. Liu, H. Xu, J. Zhang, S. Wang, Z. Liu and B. Tang, *Chem. Commun.*, 2019, **55**, 9661–9664.
24 D. Sun, D. Meng, Y. Cai, B. Fan, Y. Li, W. Jiang, L. Huo, Y. Sun and Z. Wang, *J. Am. Chem. Soc.*, 2015, **137**, 11156–11162.
25 J. Zhang, Y. Li, J. Huang, H. Hu, G. Zhang, T. Ma, P. C. Y. Chow, H. Ade, D. Pan and H. Yan, *J. Am. Chem. Soc.*, 2017, **139**, 16092–16095.
26 E. Kozma, W. Mróz, F. Villafiorita-Monteleone, F. Galeotti, A. Andicsová-Eckstein, M. Catellani and C. Botta, *RSC Adv.*, 2016, **6**, 61175–61179.
27 G. Li, Y. Zhao, J. Li, J. Cao, J. Zhu, X. W. Sun and Q. Zhang, *J. Org. Chem.*, 2015, **80**, 196–203.
28 M. Matussek, M. Filapek, P. Gancarz, S. Krompiec, J. Grzegorz Małecki, S. Kotowicz, M. Siwy, S. Maćkowski, A. Chrobok, E. Schab-Balcerzak and A. Słodek, *Dyes Pigm.*, 2018, **159**, 590–599.
29 L. Zong, Y. Gong, Y. Yu, Y. Xie, G. Xie, Q. Peng, Q. Li and Z. Li, *Sci. Bull.*, 2018, **63**, 108–116.
30 S. V. Dayneko, A. D. Hendsbee and G. C. Welch, *Small Methods*, 2018, **2**, 1800081.
31 J. R. C. Smirnov, A. Sousaraei, M. R. Osorio, S. Casado, J. J. Hernández, L. Wu, Q. Zhang, R. Xia, D. Granados, R. Wannemacher, I. Rodriguez and J. Cabanillas-Gonzalez, *npj Flexible Electron.*, 2019, **3**, 17.
32 J. H. Ahn, C. Wang, I. F. Perepichka, M. R. Bryce and M. C. Petty, *J. Mater. Chem.*, 2007, **17**, 2996.
33 D. de Azevedo, J. N. Freitas, R. A. Domingues, M. M. Faleiros and T. D. Z. Atvars, *Synth. Met.*, 2017, **233**, 28–34.
34 K. Kwak, K. Cho and S. Kim, *Sci. Rep.*, 2013, **3**, 2787.
35 M. Gioti, D. Kokkinos, C. I. Chaidou, A. Laskarakis, A. K. Andreopoulou, J. K. Kallitsis and S. Logothetidis, *Phys. Status Solidi*, 2016, **213**, 2947–2953.
36 A. C. M. Colella, J. Griffin, J. Kingsley, N. Scarratt, B. Luszczynska and J. Ulanski, *Micromachines*, 2019, **10**, 53.
37 C. Würth, M. Grabolle, J. Pauli, M. Spieles and U. Resch-Genger, *Nat. Protoc.*, 2013, **8**, 1535–1550.
38 F. J. Céspedes-Guirao, S. García-Santamaría, F. Fernández-Lázaro, A. Sastre-Santos and H. J. Bolink, *J. Phys. D: Appl. Phys.*, 2009, **42**, 105106.